ELSEVIER

Finite element modeling for analysis of electroluminescence and infrared images of thin-film solar cells

Matthias Diethelm [a,*], Lieven Penninck [b], Markus Regnat [c], Ton Offermans [d], Birger Zimmermann [e], Christoph Kirsch [c], Roman Hiestand [b], Stéphane Altazin [b], Beat Ruhstaller [b,c,**]

[a] Empa, Swiss Federal Laboratories for Materials Science and Technology, Laboratory for Functional Polymers, 8600 Dübendorf, Switzerland
[b] Fluxim AG, Katharina-Sulzer-Platz 2, 8400 Winterthur, Switzerland
[c] Zurich University of Applied Sciences, Institute of Computational Physics, Technikumstrasse 9, 8401 Winterthur, Switzerland
[d] CSEM Center Muttenz, Tramstrasse 99, 4132 Muttenz, Switzerland
[e] Fraunhofer Institute for Solar Energy Systems ISE, Heidenhofstrasse 2, 79110 Freiburg, Germany

ARTICLE INFO

ABSTRACT

Sheet resistance losses and local defects are challenges faced in solar module fabrication and upscaling processes. Commonly used investigation tools are non-invasive optical and thermal imaging techniques, such as electroluminescence, photoluminescence as well as illuminated and dark infrared imaging. Here, we investigate the potential of computationally efficient finite element simulation of solar cells and modules by considering planar electrodes coupled by a local current–voltage coupling law. Sheet resistances are determined by fitting current simulation results of an OPV solar cell to electroluminescence imaging data. Moreover, a thermal model is introduced that accounts for Joule heating due to an electrothermal coupling. A direct comparison of simulated temperature maps to measured infrared images is therefore possible. The electrothermal model is successfully validated by comparing measured and simulated temperature profiles across four interconnected organic solar cells of a mini-module. Furthermore, the influence of shunts on the thermal behavior of OPV modules is investigated by comparing electrothermal simulation results to dark lock-In IR thermography images.

1. Introduction

An important engineering challenge for large scale deployment of novel solar cell technologies is preserving the high power conversion efficiencies demonstrated for small cells also in large area devices such as modules with interconnected cells. This problem is faced by established silicon based technologies as well as emerging PV material systems like perovskite or organic photovoltaics. In practice the aim is to minimize the reduction in power conversion efficiency (PCE) in a PV module compared to a lab-scale device. Several effects contribute to the loss in PCE in large-area devices. First the resistivity of the transparent conductive electrode (TCE) causes a reduction of the operating voltage (Paire et al., 2011). Second, local defects will cause shunts acting as a localized current loss channels (Eder et al., 2018).

To investigate these effects, electroluminescence (EL) and infrared (IR) imaging are widely used in the PV community (Berardone et al., 2018; Ebner et al., 2015). These non-invasive techniques allow a quick and simultaneous screening of a cell or module and are thus also used in production (Du et al., 2017). Electroluminescence results from photons emitted due to radiative recombination of holes and electrons that form part of the current flowing through the local diode, and is therefore approximately proportional to the local current (Kalinowski, 2000). Because the diode films are very thin compared to the lateral dimension, the diode current and EL signal are localized and lateral current flow is only in the TCE. Potential drops across TCEs due to the sheet resistance can therefore be deduced from the EL image (Paire et al., 2010). Shunts are distorting the EL image since they draw a large amount of current, leading to a strong lateral voltage drop in the surrounding of the shunt an thus reduced current and EL signal in the vicinity (Kasemann et al., 2008). The large local current density through a shunt results in a high power dissipation and thus in significant local heating. Therefore, infrared imaging is ideally suited and widely used (Karl et al., 2019).

Dark Lock-In Thermography (DLIT) where a pulsed current is applied is especially useful for accurate shunt localization (Ebner et al., 2015).

Further information can be extracted from EL and infrared imaging techniques by combining them with computational methods. An analytical diode model was used to obtain the TCE sheet resistance from local EL images of CIGS solar cells (Paire et al., 2011). EL images of polymer solar cells were compared in a similar way to equivalent circuit models (Seeland et al., 2012). 2D grid SPICE simulation are widely used to simulate solar cells or modules by a network of equivalent circuit macromodels, where the 2D electrodes are mapped as a network of resistors (Pieters, 2011). Photoluminescence images (PL), EL and DLIT images were thereby compared to simulations to extract information about the local properties of the diode and shunt behavior (Gerber et al., 2015; Kasemann et al., 2008). The drawback of this method is that a refinement of the network, e.g. for corners or shunts, requires a change in the network topology, and thermal simulation requires an additional equivalent circuit (Lanz et al., 2013). This can be solved by using a finite element method (FEM), where the simulation domain is represented by smaller elements with the same representation for electrical and thermal simulation, and a refinement step is a change of discretization only. Moreover, the design of customized geometries is easily achieved with parametrized geometry definitions or CAD software features. The electrodes could be mapped by 3D finite element models (Lyu et al., 2012), but they quickly become prohibitively expensive in computation memory and time (Kirsch et al., 2017). This is because of the dimensions and aspect ratio of the problem: The solar cell stack is a few hundreds of nanometers to a few micrometers thick while the lateral area is at least on the order of cm^2. The required small mesh size for the stack tends to lead then to a huge mesh number for the lateral area. However, because of this aspect ratio, the 3D problem can be reduced to two 2D electrodes connected by a 1D model. This is the same approximation as assuming lateral current flow only within the electrodes. This concept was implemented in Griddler (Wong, 2013), which was fitted to PL images in order to extract recombination parameters of the diode model and investigate lateral variations (Li et al., 2018). General purpose FEM software was previously employed for the electrical analysis of shunts and defects in thin film solar cell modules (Fecher et al., 2014; Lanz et al., 2013). We developed a dedicated simulation software called Laoss for large-area device simulation with the same 2D + 1D concept. In addition to electrical modeling it is able to do thermal and optical device modeling (Laoss 4.0 by Fluxim). Electrothermal modeling of solar cells or modules is so far rather underexploited, since only very few compared simulation results to measurements (Lanz et al., 2013; Nardone and Lee, 2018; Silverman et al., 2015). Here, we investigate the potential of full

solar cell and module geometry simulation of lateral current, voltage and temperature maps and the possibility of extracting information about material parameters from fitted EL, infrared and DLIT images.

2. Results and discussion

2.1. Simulation model

In the electrical model of Laoss as shown in Fig. 1a, the 3D problem is simplified by assuming that all lateral flow of current is carried by the thin film electrodes, i.e. by the cathode and anode of the solar cell. Inside the thin film semiconductor stack the current is assumed to flow strictly perpendicular to the planar electrode. These two assumptions are justified since the conductivity of the electrode materials is significantly higher than the conductivity of the semiconductor material and the thickness of the semiconductor stack is orders of magnitude lower than the lateral dimensions of the device even for small lab-scale devices of a few mm^2.

In steady state the charge continuity equation in the top electrode is given by

$$\nabla \vec{J}_{top} = -j_{z,top}, \tag{1}$$

where $j_{z,top}$ is the current density flowing vertically from the top electrode to the bottom and the vector $\vec{J}_{top}$ is the two-dimensional current density flowing in the plane of the electrode. Thus, divergence of the current in the electrode plane is only non-zero if current is flowing vertically between the electrode planes, i.e. if there is a coupling law. With Ohm's law $\vec{J} = \sigma \vec{E}$ and the electric field $\vec{E} = -\nabla V$ we arrive at the current conservation law in the (top) electrode domain

$$\frac{1}{R_{\square,top}} \Delta \vec{V}_{top} = j_{z,top}, \tag{2}$$

where $\vec{V}_{top}$ is the in z direction averaged electric potential in the top electrode, $R_{\square,top} = \frac{1}{\sigma * d}$ is the sheet resistance of the top electrode with unit $\Omega/\square$ and top electrode thickness d, and $\Delta = \nabla * \nabla$ is the Laplacian operator. An analogous continuity expression is found for the bottom electrode.

The term $j_{z,top}$ depends on the potential difference between the top and bottom electrode and provides thus a coupling between the differential equations for $\vec{V}_{top}$ and $\vec{V}_{bot}$. We discretize and solve the coupled differential equations (Eq. (2)) in each of the two electrodes by the finite
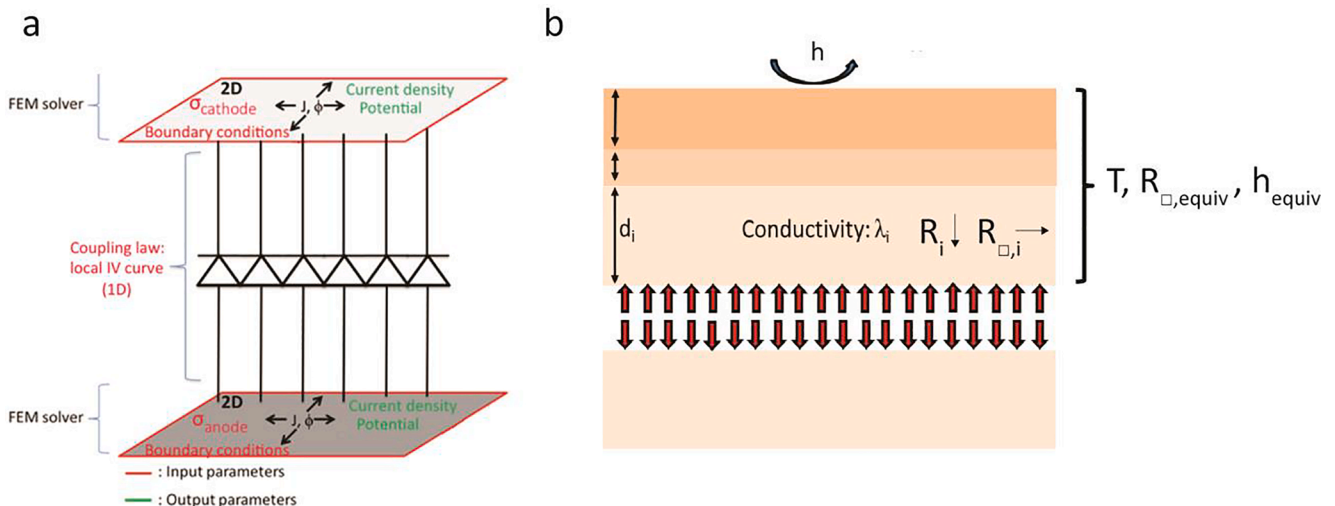

Fig. 1. Model schematics. Schematic of the 2 + 1D electrical (a) and thermal (b) model implemented in the simulation software Laoss (Laoss 4.0 by Fluxim).

element method via Newton's method.

These continuity equations are valid for an arbitrary function $j_{z,top}(V_{top} - V_{bot})$. This electrical coupling law is zero if the bottom electrode is not connected to the top, for example for the contact pads on each side of the module. On the other hand, it can be ohmic for the case of a shunt, or the interconnection between cells of a module. Lastly, the coupling law for the active areas of the solar cells is a diode model, or a locally measured JV curve of a cell with a small area as it is the case in this work, typically below 1 mm^2. As boundary conditions we specify the potential at the contact points of the solar cell and a Neumann condition of zero current density at all other outward boundaries of the electrodes.

The temperature distribution is modeled as shown in Fig. 1b considering equivalent thermal sheet resistance $R_{\square,equiv}$ of the stacks above the active layer as well as below. They are calculated by the individual layer thermal sheet resistances $R_{\square} = \frac{1}{\lambda d}$ and vertical thermal resistances $R = \frac{1}{\frac{1}{d}}$, where λ is the thermal conductivity of the material and d the thickness of the layer. Furthermore, an equivalent heat transfer coefficient h_{equiv} is calculated in Eq. (4) from the heat transfer coefficient to air h and the sum of the vertical thermal resistances R_{tot}. A full example calculation for the multi-layer parameters is given in Table S1.

$$\frac{1}{R_{\square,equiv}} = \sum_i \frac{1}{R_{\square,i}} \left[\left(\frac{h_{equiv}}{h} + h_{equiv} \sum_{n=1}^{i-1} R_n + \frac{h_{equiv} R_i}{2} \right) \right], \quad (3)$$

$$h_{equiv} = \frac{h}{1 + R_{tot} h}. \quad (4)$$

The temperature T in the stack above and below the active layer is then calculated similar to Eq. (2) by

$$-\frac{1}{R_{\square,equiv}} \Delta T = \Phi_{Joule_{electrode}} + \Phi_{Joule_{diode}} + \Phi_{conduction_{diode}} - \Phi_{exchange_{environment}}, \quad (5)$$

considering the different heat fluxes $\Phi([W/m^2])$: Joule heating of the current flowing lateral in the electrode ($\Phi_{Joule_{electrode}}$), the current flowing perpendicular in between the electrodes ($\Phi_{Joule_{diode}}$) and the heat flow coming from the other electrode ($\Phi_{conduction_{diode}}$). The heat loss through the environment is included by

$$\Phi_{exchange_{environment}} = h_{equiv} \left(T_{top} - T_{ambient} \right)$$

where the equivalent heat transfer coefficient h_{equiv} represents the sum of the convective and radiative exchanges. The flux ($\Phi_{Joule_{diode}}$) would also include absorbed light power. However, the modules in the thermal imaging section were measured in the dark.

The electrical and thermal model are coupled by the exponential dependence

$$e^{\frac{E_0}{k_B} \left(\frac{1}{T_0} - \frac{1}{T} \right)}$$

with an activation energy E_0 of 0.2 eV, which is the factor that leads to an increase of the diode current measured at the temperature T_0, depending on the increased temperature T. Both models are solved consistently with the finite element method.

2.2. Electroluminescence imaging

As input for the simulation of the OPV cell, typical sheet resistances as shown in Table 1 were used. The JV-curve of a P3HT:PCBM OPV cell with an area of 0.04 cm^2 was measured and used as local JV coupling law (Fig. S1).

Fig. 2a shows an EL measurement of the OPV cell which is compared to the simulated current density through the cell in Fig. 2b. A global intensity reduction from left to right can be observed in both images because the bottom aluminum cathode is contacted at the left side only as shown in Fig. S2. This leads to a resistive voltage drop from left to

Table 1
Input sheet resistances.

Material	Electrical sheet resistance $\Omega/\square$
Gold	0.24
PEDOT:PSS	448
Aluminum	0.4

Input sheet resistances for the simulation shown in Fig. 2. They are calculated from the resistivity divided by the thickness of the respective layer.

right and thus decreasing current and luminance. In other words, the cell area closer to the short edge contact on the left experiences a vertical potential difference that is closer to the applied terminal voltage, whereas the area far right experiences a net potential difference that is reduced by the lateral voltage drop. As the applied current of 100 mA is roughly 10 times higher than the typical short circuit current (I_{SC}) value, this image shows a more drastic gradient than will be present under operating conditions. This will be analyzed in more detail below.

For better comparison of the data in Fig. 2, Fig. S3 shows the cross-sections of the EL measurement (a) and the simulated current density profile (b) along the x-axis. Besides the global intensity decay from left to right, some additional features are visible. On the one hand, at the location of the metal grid lines every 1 mm, the measured EL signal is sharply reduced because the emitted light is absorbed or shaded by the metal grid. The simulated current density on the other hand reaches a local maximum below every individual highly conductive metal grid line, and in between them the potential and thus the current density drops due to the high PEDOT:PSS sheet resistance.

In Fig. 3a cross-sections of the simulated current density distributions are compared to the EL intensity measurements at driving currents of 10, 30, 50 and 100 mA, which correspond roughly to $1\times$, $3\times$, $5\times$, and $10\times$ I_{SC} of the device under 1 sun illumination. The simulated and measured applied voltages corresponding to these currents are compared in Table 2. The EL cross-sections are normalized by the highest grid EL signal count value 6827 (measured at 100 mA). The simulated current density curves were scaled by the factor of 127 mA. Only the 100 mA current simulation profile was scaled with a lower factor (116 mA). Except for the 100 mA profiles, the assumption that the EL signal is proportional to the current density through the diode seems thus to hold. This discrepancy is discussed at the end of this chapter. Furthermore, the global decrease in EL intensity from left to right is well reproduced except in the region from 14 mm to 22 mm. The drop in EL intensity in between 2 grid lines matches well between measurement and simulation for the 100 mA profiles in the region from 1 mm to 6 mm.

To investigate the discrepancies in simulation and measurement, the different resistances in the device were individually altered and simulated. Fig. 3b shows the 100 mA current density profiles for different aluminum back contact and PEDOT:PSS front contact sheet resistances. We find distinct behavior for varying either of these two quantities. The higher the bottom electrode sheet resistance (aluminum), the steeper the decay along the cell (left to right). The higher the top electrode (sheet resistance) PEDOT:PSS, the higher the voltage and thus current drop in between two grid lines. In principle fitting of the simulated profiles therefore enables the determination of the PEDOT:PSS conductivity by matching the drop in between grid lines of the simulated current to the EL profile. The gold grid which absorbs or shadows the emitted light directly below the grid complicates a fit because a smaller range is available for the curve-fitting. In terms of the device layout it can be seen from the 10 mA curve in Fig. 3a, that there is nearly no local variation of current, neither due to the PEDOT:PSS resistance nor due to the aluminum resistance, which means that the cell is not severely limited by the overall series resistance of the electrodes under operating conditions, where the current is on a similar level.

Fig. 3c shows the influence of the gold electrode. The charge carriers are collected from the grid lines by the grid bar on top that surrounds the
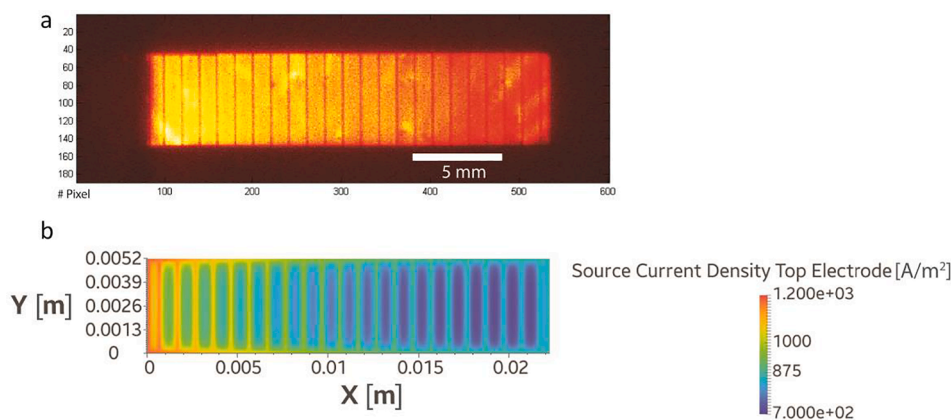
Fig. 2. JV and temperature simulations. Electroluminescence image measurement (a) and simulated current density distribution (b) for an OPV cell with a metal finger grid while a total current of 100 mA (ca. 10× I$_{SC}$) flowing through the device, both for measurement and simulation.
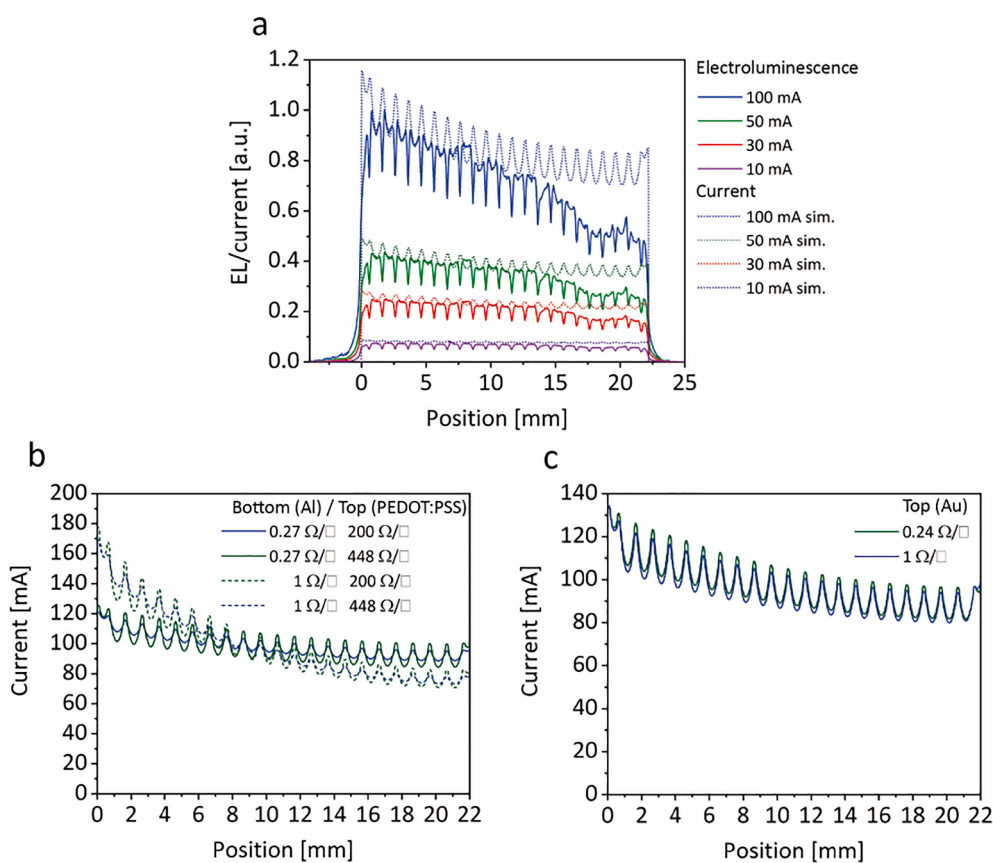

Fig. 3. Electroluminescence measurement and current simulation. EL measurement and simulation comparison (a), effect of electrode resistance on lateral current profile (b) and (c) gold electrode sheet resistance change from 0.24 Ω/□ (green) to 1 Ω/□ (blue) at a total current of 100 mA.

Table 2
Simulated and measured applied voltage for different currents.

Current [mA]	Voltage measured [V]	Voltage simulated [V]
100	1.17	1.12
50	0.94	0.95
30	0.83	0.86
10	0.69	0.73

cell which is connected to the anode as shown in Fig. S2, so no influence along the x axis can be observed. Therefore the sheet resistance variation does not have a big impact, also because the resistance is relatively low.

Regarding the 8.7% higher correction factor for the 100 mA simulation: When integrating the EL signals from Fig. 3a, the ratios are 8.9:28.5:47.6:100 for the respective measurement current of 10:30:50:100 mA. This partly reflects the correction factor, since the 30 mA and 50 mA EL measurement are proportional (28.5:47.6 = 29.9:50 ≈ 30:50), but the integrated EL signal for the 100 mA measurement is 5% higher than its expected value when assuming a linear current-to-EL relation (47.6:100 = 50:105). Since rather a decrease of current-to-EL efficiency is expected for such high current levels of roughly 100 mA at an area of 1.1 cm² (roll-off as described in Liu et al., 2015), we assume measurement inaccuracy to be the reason and do not further investigate it.

To understand the inconsistencies observed in Fig. 3a, the findings from the sheet resistance variation give a hint. One explanation for the steeper decay in the region from 14 mm to 18 mm can be a change in the sheet resistance of the aluminum back electrode, judged from Fig. 3b. While the resistivity of aluminum will most likely not change, an unintentionally thinner layer can lead to a higher sheet resistance. However, the slight increase of electroluminescence from 18 mm to 22 mm is countering the hypothesis of voltage loss due to higher resistance, since there would be no explanation for a sudden increase in potential drop. An alternative possibility is a varying local diode behavior due to non-uniform thickness of the deposited semiconducting layer. Delamination or an insulating oxide layer in between the aluminum electrode and organic layer can lead as well to a similar result (Schaer et al., 2001; Züfle et al., 2015). Finally, the question arises whether shunts could be the reason for the observed behavior. From the EL image, it is hard to judge whether this is the case. Overall, the simulated current density maps agree well with the measured EL image intensity maps and allowed us to determine the sheet resistances of PEDOT:PSS as well as the aluminum electrode, as it was done in other work (Helbig et al., 2010). In the following section, the investigation of shunts is introduced with thermal imaging combined with simulation using the finite element method.

2.3. Thermal imaging

A powerful method to investigate shunts is thermal imaging because the higher current density at a local shunt leads to higher local temperature due to Joule heating. In this section we investigate a mini-module consisting of four interconnected, printed organic solar cells that suffer from imperfect layer deposition and film formation. Images taken by an infrared camera reveal the lateral temperature distribution as displayed in Fig. 4a, where shunts appear as bright spots. The images were taken after the steady temperature was reached after roughly 1 min as shown in the time-dependent cell temperature measurement provided in Fig. S5. In IR thermography, lock-in techniques are a popular alternative to acquiring steady-state IR images to improve signal to noise ratios. A direct comparison of measured and simulated lock-in thermography images demands a FEM solver that can compute the complex temperature with amplitude and phase information at the given AC modulation frequency, however. In the module under investigation, shunts with different severity are present. It seems that a shunt on the bottom right corner with the brightest appearance is dominating the electrical and thus thermal behavior of the whole sub cell. To prove this hypothesis, the part of the module containing this shunt was cut such that the four sub cells remained operating with a reduced width. The remaining module showed a more homogeneous temperature distribution as displayed in Fig. S4. The effect can also be observed in the current–voltage measurement in Fig. 5a. After removing the part with the shunt, the voltage of the whole module at a current density e.g. of 2 mA/cm^2 shifts from 2.6 V to 3.2 V. This increase of roughly 25% shows that the one sub cell out of four was indeed shunted before and therefore not contributing to the overall module voltage. There are remaining shunts, but they are apparently not as strongly shorting as the shunt that was removed by cutting.

In order to judge the influence of shunts on the current and temperature profile, a thermal model is set up and compared to the infrared image data. The geometry of the module with four sub cells was included as shown in Fig. S6. To get a better contrast of the shunts, dark lock-in thermography (DLIT) was measured on the module (Fig. S7), and one shunt per sub cell was included in the modeled mini-module,
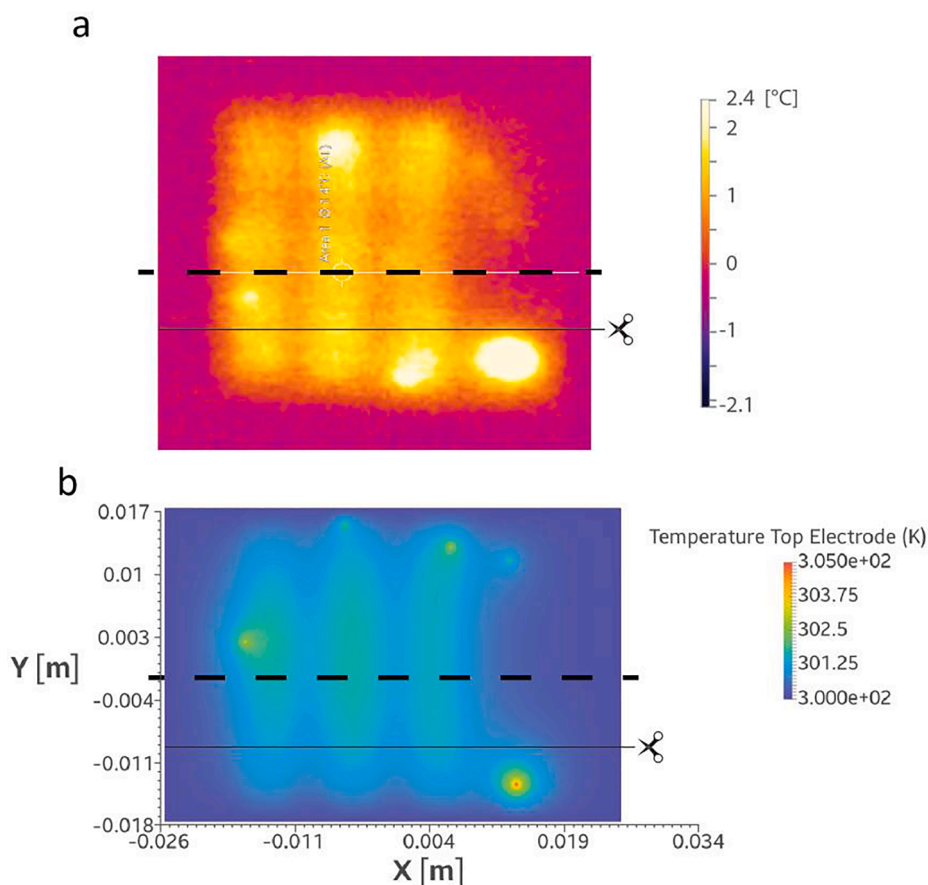

Fig. 4. Comparison of temperature simulation to infrared measurement. Infrared image measurement (a) and simulated temperature distribution (b) of the full module at a current of 10 mA (5.6 mA/cm^2).
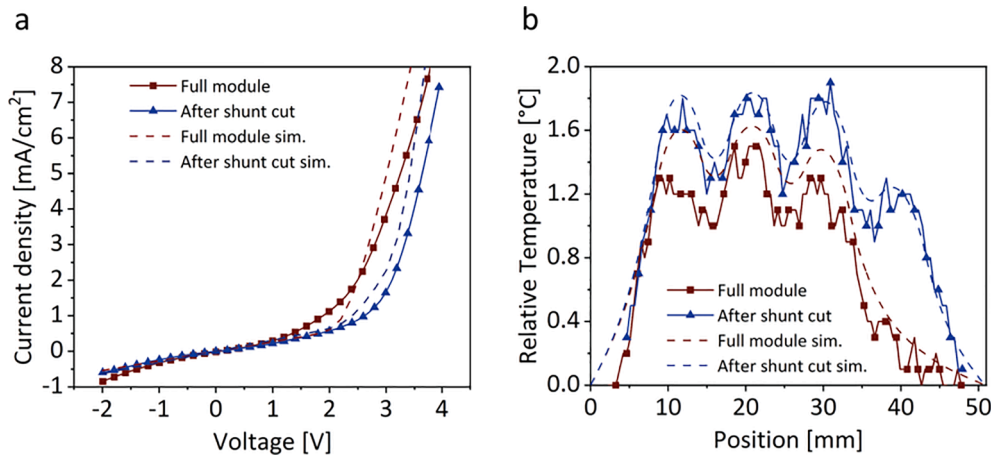
Fig. 5. JV and temperature measurement to simulation comparison. Measurement (solid lines) and simulation (dashed lines) of JV curves of the OPV module (a) before and after removing the shunt by cutting. Cross-section of IR thermography image and simulated temperature profile given relative to the ambient temperature (b).

denoted as no. 1–4. In addition, the heavily shorting shunt of the forth sub cell was included, denoted as no. 5. For shunt no. 1–3 we assume a conductivity from top to bottom of 0.55 S/m, shunt no. 4 is modeled with 0.22 S/m and shunt no. 5 with 3.65 S/m. As coupling law for the active cells a local JV curve was measured (Fig. S8) on separately fabricated cells with an area below 1 mm². The electrical and thermal sheet resistances used for different subdomains are summarized in Table 3. The electrical sheet resistances are calculated from the resistivity divided by the thickness of the respective layer. The thermal sheet resistances are calculated as described in the model section. The underlying thermal conductivities for the different layers and an example calculation for the effective resistances are shown and described in the supporting information in Table S1.

The simulated lateral temperature distribution is shown in Fig. 4b, where the similarity to the infrared image is obvious. Note that not all visible shunts are simulated, but at least one per cell. The line plot comparison for a cross-section as defined by the dashed line in the image is shown in Fig. 5b. For the full module, there is a slight overestimation of the temperature by 15%, the temperature distribution trend, however, is captured well. After the severest module shunt is removed by cutting, the agreement of the infrared measurement and temperature simulation is striking. The lateral measurement and simulation of the cut module are shown in Fig. S9. In Fig. 5a, the same JV curve voltage shift before and after module shunt cut is visible in the simulation as in the measurement. This strengthens the hypothesis of the dominating effect of only one shunt. Although less prominent, the simulation catches also the trend of increased temperature after cutting the module. One reason is simply that the same current level of 10 mA was chosen before and after the cutting, leading to higher current density for the cut module

Table 3
Input electrical and thermal sheet resistances per subdomain of the simulation.

Subdomain	Electrical sheet resistance ($\Omega/\square$)		Thermal sheet resistance (K/W/$\square$)	
	Bottom	Top	Bottom	Top
Active area only	35	50	20525	3349
Metal finger	35	0.41	20525	3141
Silver cut (P1)	0.41	1E9	20525	3367
Interconnection (P2)	0.41	0.41	20525	3141
ITO cut (P3)	1E9	50	1E9	3349

There are no metal fingers on the bottom electrode, therefore the subdomain for the metal finger contains the same parameter as the active layer bottom subdomain. The interconnections in between the 4 cells contain the sections "P1 cut" and "ITO unconnected" and is interconnected by "Interconnection". The separations are modeled as very high sheet resistance (1E9 $\Omega/\square$).

with reduced area, and thus higher temperature. The area decrease is 21.25%, and the increase of measured temperature in between 7 mm and 35 mm (Fig. 5b) is 32% on average.

To understand this discrepancy, simulations of the cut module only are carried out, with and without some or all of the remaining shunts no. 1–4. Fig. 6a shows the simulated JV curves where all shunts are active (blue, solid), and without any shunts (green, solid). The major influence of removing the shunts in the model is the absence of the parallel conductance, which can be calculated from the slope at zero voltage. The temperature profiles at 7.1 mA/cm² for the case with all four and without any shunts are displayed in Fig. 6b. Although the applied voltage is very similar in both cases (3.61 V and 3.72 V), a big temperature discrepancy can be observed. This seems counterintuitive because shunts are associated with heating. The reason is that when there are less or no shunts, more current is flowing regularly through the diode, such that the potential drop locally across the diode will also be higher, leading to higher current, power and Joule heating. It is possible that this effect contributes to the roughly 32% increase in temperature when cutting the module where only 21% can be explained by increased overall current density. Note that at the measured temperature increase of around 1.2–2 °C on average, and up to 8 °C for the shunts, we do not expect that thermal runaway (spiral up of current and temperature increase) plays a role as it was shown in other studies (Guthrey et al., 2019; Vasko et al., 2014). A simulation of the cut module with and without back coupling of the temperature is discussed in Fig. S10.

In a last step, simulations were carried out with a different number of shunts. Starting from the cut module simulation in Fig. 6a (blue, solid), shunt no. 2 was removed. For voltages after turn-on at around 2 V, the JV curve (red, dashed) is equal. However, the parallel conductance seemed to disappear completely, and the JV curve below 1 V become identical to the simulation without any shunts (green, solid). This is because with removal of shunt no. 2, the second sub cell of the module did not contain any shunt, and since it is connected in series to the other shunted sub cells, it blocks the overall shunting behavior of the module; if a voltage slightly below or above 0 V is applied, the second sub cell without shunts connected in series blocks any current that would flow through shunts from another sub cell. The two further simulations all contain at least one sub cell without shunts, therefore they all have no parallel conduction. With removal of the fourth shunt only (purple, dashed), the JV curve gets more rectangular already because shunt no. 4 has a higher conductance than shunt no. 2. If only shunt no. 3 is active (dark red, dashed), the JV is close to the case without any shunts (green, solid). These results indicate that judging the module shunt behavior from the slope at 0 V gives only a measure for the sub cell connected in series with the lowest shunt resistance, while the fill factor relates to all
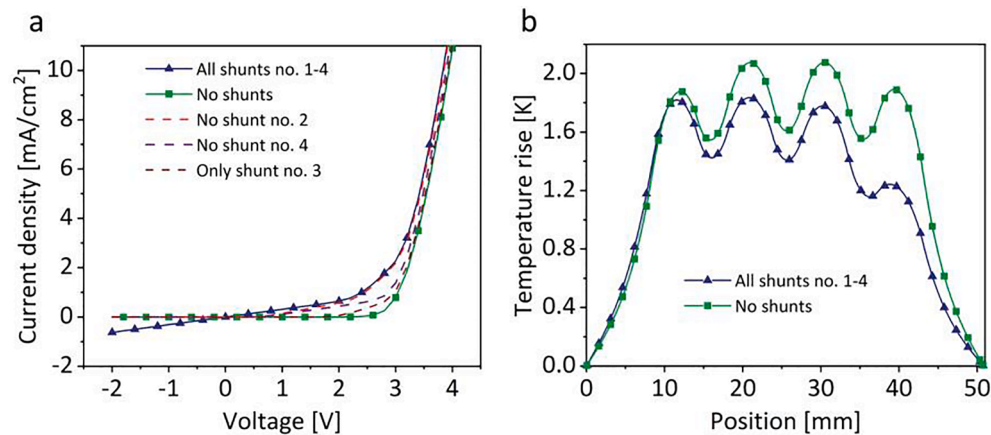
Fig. 6. JV and temperature simulations. Simulations of the cut module with varying shunts of JV curves (a) and heating profiles at a current density of 7.1 mA/cm^2 (b).

shunted sub cells because of the voltage loss in each one of them.

3. Conclusion

In this paper we demonstrated that the electrothermal behavior of large area organic solar cells of arbitrary shape can be simulated by a coupled 2 + 1D FEM approach. It allows drawing conclusions about non-uniformities by fitting the simulated current distribution to the observed EL-image profile and thereby confirming or extracting the involved material parameters. Furthermore, thermal imaging can be combined with electrothermal simulation to investigate the shunting behavior. A full picture can be gained by combination of EL and thermal imaging with simulation. By having a model that fits the electrical and thermal measurement of the large area device including shunts, the potential of the module without shunts can then be assessed. This information can be used to assist the upscaling process by predictive modeling.

4. Experimental section

The OPV cells for the electroluminescence imaging study were fabricated at Fraunhofer ISE, Freiburg, Germany, as previously described (Sapkota et al., 2014) and contain the structure aluminum (100 nm)/P3HT:PCBM/PEDOT:PSS (50 nm)/gold (100 nm). The individual solar cells have a rectangular shape with the dimension of 5×22 mm^2. They contain a gold grid parallel to the short edge with a period of 1 mm. One electrode is contacted at the short edge whereas the other electrode is contacted with a u-shaped conductive boundary containing the two long edges and the opposite short edge. The same contacting scheme is also implemented in the FEM model, as illustrated in the supplemental info. Electroluminescence (EL) images were measured using a back-illuminated Si-CCD camera with the CCD chip cooled to –70 °C. The wavelength band used (975–1100 nm) was controlled with optical long-pass filters (Reinhardt et al., 2014).

For thermal imaging, OPV mini-modules consisting of 4 cells (5×5 cm^2 substrate) connected in series were fabricated by CSEM, Muttenz, Switzerland (Offermans et al., 2018). The structure of one cell is PET foil/ITO/gold grid/ETL/active/HTL/silver grid. The ETL was obtained from GenesInk, AZO formulation DZ91007. The active OPV material was a blend of Lisicon PV-D4610 (Merck) and PCBM (Solenne) mixed in a ratio of 1:2. As HTL, a bilayer of low conductivity PEDOT:PSS (Clevios P VP AI4083) and high conductivity PEDOT:PSS (AGFA HILHC52) was used. Dark lock-in thermography and infrared images were acquired with an Optris PI 160 infrared camera (Optris GmbH) inside a glovebox under nitrogen atmosphere at Zurich University of Applied Sciences (ZHAW). Cutting of the module was done with a scissor, which was possible due to the flexible PET foil substrate.

Declaration of Competing Interest

The authors declare that they have no known competing financial interests or personal relationships that could have appeared to influence the work reported in this paper.

Appendix A. Supplementary material

Supplementary data to this article can be found online at https://doi.org/10.1016/j.solener.2020.08.058.

References

Berardone, I., Paggi, M., Lopez Garcia, J., 2018. Analysis of electroluminescence and infrared thermal images of monocrystalline silicon photovoltaic modules after 20 years of outdoor use in a solar vehicle. Sol. Energy 173, 478–486. https://doi.org/10.1016/j.solener.2018.07.055.

Du, B., Yang, R., He, Y., Wang, F., Huang, S., 2017. Nondestructive inspection, testing and evaluation for Si-based, thin film and multi-junction solar cells: An overview. Renew. Sustain. Energy Rev. 78, 1117–1151. https://doi.org/10.1016/j.rser.2017.05.017.

Ebner, R., Kubicek, B., Ujvari, G., Novalin, S., Rennhofer, M., Halwachs, M., 2015. Optical characterization of different thin film module technologies. Int. J. Photoenergy 2015. https://doi.org/10.1155/2015/159458.

Eder, G.C., Voronko, Y., Hirschl, C., Ebner, R., Újvári, G., Mühleisen, W., 2018. Non-destructive failure detection and visualization of artificially and naturally aged PV modules. Energies 11, 1–14. https://doi.org/10.3390/en11051053.

Fecher, F.W., Pérez Romero, A., Brabec, C.J., Buerhop-Lutz, C., 2014. Influence of a shunt on the electrical behavior in thin film photovoltaic modules - A 2D finite element simulation study. Sol. Energy 105, 494–504. https://doi.org/10.1016/j.solener.2014.04.011.

Gerber, A., Huhn, V., Tran, T.M.H., Siegloch, M., Augarten, Y., Pieters, B.E., Rau, U., 2015. Advanced large area characterization of thin-film solar modules by electroluminescence and thermography imaging techniques. Sol. Energy Mater. Sol. Cells 135, 35–42. https://doi.org/10.1016/j.solmat.2014.09.020.

Guthrey, H., Nardone, M., Johnston, S., Liu, J., Norman, A., Moseley, J., Al-Jassim, M., 2019. Characterization and modeling of reverse-bias breakdown in Cu(In, Ga)Se2 photovoltaic devices. Prog. Photovoltaics Res. Appl. 27, 812–823. https://doi.org/10.1002/pip.3168.

Helbig, A., Kirchartz, T., Schaeffler, R., Werner, J.H., Rau, U., 2010. Quantitative electroluminescence analysis of resistive losses in Cu(In, Ga)Se2 thin-film modules. Sol. Energy Mater. Sol. Cells 94, 979–984. https://doi.org/10.1016/j.solmat.2010.01.028.

Kalinowski, J., 2000. Physics of Organic Electroluminescence. In: Kajzar, F., Agranovich, M.V. (Eds.), Multiphoton and Light Driven Multielectron Processes in Organics: New Phenomena, Materials and Applications: Proceedings of the NATO Advanced Research Workshop on Multiphoton and Light Driven Multielectron Processes in

Organics: New Phenomena, Materials A. Springer Netherlands, Dordrecht, pp. 325–344. https://doi.org/10.1007/978-94-011-4056-0_24.

Karl, A., Osvet, A., Vetter, A., Maisch, P., Li, N., Egelhaaf, H.J., Brabec, C.J., 2019. Discriminating bulk versus interface shunts in organic solar cells by advanced imaging techniques. Prog. Photovolt. Res. Appl. 27, 460–468. https://doi.org/10.1002/pip.3121.

Kasemann, M., Grote, D., Walter, B., Kwapil, W., Trupke, T., Augarten, Y., Bardos, R.A., Pink, E., Abbott, M.D., Warta, W., 2008. Luminescence imaging for the detection of shunts on silicon solar cells. Prog. Photovolt. Res. Appl. 16, 297–305. https://doi.org/10.1002/pip.812.

Kirsch, C., Altazin, S., Hiestand, R., Beierlein, T., Ferrini, R., Offermans, T., Penninck, L., Ruhstaller, B., 2017. Electrothermal simulation of large-area semiconductor devices. Int. J. Multiphys. 11, 127–136. https://doi.org/10.21152/1750-9548.11.2.127.

Lanz, T., Bonmarin, M., Stuckelberger, M., Schlumpf, C., Ballif, C., Ruhstaller, B., 2013. Electrothermal finite-element modeling for defect characterization in thin-film silicon solar modules. IEEE J. Sel. Top. Quantum Electron. 19, 1–8. https://doi.org/10.1109/JSTQE.2013.2250259.

Laoss 4.0 by Fluxim, Switzerland, www.fluxim.com, 2020.

Li, M., Wong, J., Chen, N., Aberle, A.G., Stangl, R., 2018. Determination of metallization-induced recombination losses of screen-printed silicon solar cell contacts and their dependence on the doping profile. IEEE J. Photovoltaics 8, 1470–1477. https://doi.org/10.1109/JPHOTOV.2018.2866177.

Liu, S., Ho, S., Chen, Y., So, F., 2015. Passivation of metal oxide surfaces for high-performance organic and hybrid optoelectronic devices. Chem. Mater. 27, 2532–2539. https://doi.org/10.1021/acs.chemmater.5b00129.

Lyu, H.K., Woo, S.H., Jeong, S., Kim, K.P., Shin, J.K., 2012. Investigation of power loss and device efficiency using a three-dimensional finite element simulation on organic solar cell geometry. Sol. Energy Mater. Sol. Cells 96, 66–70. https://doi.org/10.1016/j.solmat.2011.09.003.

Nardone, M., Lee, H.C., 2018. Electrothermal Simulation of Si Cells with Defects. In: 2018 IEEE 7th World Conference on Photovoltaic Energy Conversion (WCPEC). IEEE, pp. 3208–3213. https://doi.org/10.1109/PVSC.2018.8547902.

Offermans, T., Fricke, S., Ferrini, R., Mercier, C., Penninck, L., Ruhstaller, B., Cruchon, B., Pierron, P., Duché, D., Escoubas, L., Simon, J.-J., 2018. Towards customized free-form OPV modules. In: LOPEC München 2018.

Paire, M., Lombez, L., Guillemoles, J.F., Lincot, D., 2011. Measuring sheet resistance of CIGS solar cell's window layer by spatially resolved electroluminescence imaging. Thin Solid Films 519, 7493–7496. https://doi.org/10.1016/j.tsf.2010.12.214.

Paire, M., Lombez, L., Guillemoles, J.F., Lincot, D., 2010. Toward microscale Cu(In, Ga)Se2 solar cells for efficient conversion and optimized material usage: Theoretical evaluation. J. Appl. Phys. 108 https://doi.org/10.1063/1.3460629.

Pieters, B.E., 2011. Spatial modeling of thin-film solar modules using the network simulation method and SPICE. IEEE J. Photovolt. 1, 93–98. https://doi.org/10.1109/JPHOTOV.2011.2160524.

Reinhardt, J., Grein, M., Bühler, C., Schubert, M., Würfel, U., 2014. Identifying the Impact of Surface Recombination at Electrodes in Organic Solar Cells by Means of Electroluminescence and Modeling. Adv. Energy Mater. 4, 1400081. https://doi.org/10.1002/aenm.201400081.

Sapkota, S.B., Spies, A., Zimmermann, B., Dürr, I., Würfel, U., 2014. Promising long-term stability of encapsulated ITO-free bulk-heterojunction organic solar cells under different aging conditions. Sol. Energy Mater. Sol. Cells 130, 144–150. https://doi.org/10.1016/j.solmat.2014.07.004.

Schaer, M., Nüesch, F., Berner, D., Leo, W., Zuppiroli, L., 2001. Water Vapor and Oxygen Degradation Mechanisms in Organic Light Emitting Diodes. Adv. Funct. Mater. 11, 116–121. https://doi.org/10.1002/1616-3028(200104)11:2<116::AID-ADFM116>3.0.CO;2-B.

Seeland, M., Rösch, R., Muhsin, B., Gobsch, G., Hoppe, H., 2012. Electroluminescence as characterization tool for polymer solar cells and modules. Energy Procedia 31, 167–172. https://doi.org/10.1016/j.egypro.2012.11.179.

Silverman, T.J., Deceglie, M.G., Sun, X., Garris, R.L., Alam, M.A., Deline, C., Kurtz, S., 2015. Thermal and electrical effects of partial shade in monolithic thin-film photovoltaic modules. In: 2015 IEEE 42nd Photovolt. Spec. Conf. PVSC 2015 5, 1742–1747. https://doi.org/10.1109/PVSC.2015.7355668.

Vasko, A.C., Vijh, A., Karpov, V.G., 2014. Hot spots spontaneously emerging in thin film photovoltaics. Sol. Energy 108, 264–273. https://doi.org/10.1016/j.solener.2014.07.010.

Wong, J., 2013. Griddler: Intelligent computer aided design of complex solar cell metallization patterns. Conf. Rec. IEEE Photovolt. Spec. Conf. 933–938 https://doi.org/10.1109/PVSC.2013.6744296.

Züfle, S., Neukom, M.T., Altazin, S., Zinggeler, M., Chrapa, M., Offermans, T., Ruhstaller, B., 2015. An effective area approach to model lateral degradation in organic solar cells. Adv. Energy Mater. 5, 1–9. https://doi.org/10.1002/aenm.201500835.